Optimized impedance matching and enhanced attenuation by heteroatoms doping of yolk-shell CoFe$_2$O$_4$@HCN as highly efficient microwave absorbers

Chunhao Wan [a], Jiayi Wang [a], Zexuan Li [a], Shansheng Yu [a], Xiaoyi Wang [b,**], Hongwei Tian [a,*]

[a] *Key Laboratory of Automobile Materials of MOE and School of Materials Science and Engineering, Jilin University, Changchun, 130012, China*
[b] *Key Laboratory of Optical System Advanced Manufacturing Technology, Changchun Institute of Optics, Fine Mechanics and Physics, Chinese Academy of Sciences, Changchun, 130033, China*

A B S T R A C T

Microwave absorbing (MA) materials with yolk-shell structures have been extensively studied in impedance matching. However, the impedance matching achieved by the complementary effect of the core and the shell does not determine the reflection of the microwaves upon the occurrence at the first incidence. The interaction between the outer layer of materials and the electromagnetic waves significantly impacts the MA properties of materials. In this study, the impedance matching improvement method of the shell structure was further explored by preparing CoFe$_2$O$_4$@HCN (honeycomb carbon with N-doping) through the hydrothermal method followed by hydrolysis, polymerization, etching, and annealing. The resulting structure with heteroatoms doping provided the novel CoFe$_2$O$_4$@HCN with excellent impedance matching and multiple loss mechanisms contributing to MA process. The absorber with a filler loading of 40% exhibited an RL$_{min}$ of −68.03 dB with a matching thickness of 2.5 mm. The efficient absorbing bandwidth reached 5.92 GHz (a change from 11.92 to 17.84 GHz) at 1.99 mm thickness. Interestingly, these findings look promising for future synthesis and application of yolk-shell structure microwave absorbers.

1. Introduction

Over the years, the development of 5G communication technology has gradually advanced along with the 6G technique, resulting in serious electromagnetic pollution [1–3]. Flying electromagnetic waves are dangerous to human health and life and interfere with the operation of electronic equipment [4,5]. To reduce the influence of electromagnetic waves, microwave absorbing (MA) materials have been widely studied in various fields as effective materials, which are divided into conduction loss type, dielectric loss type, and magnetic loss type [6]. For applications, a preeminent MA material should simultaneously satisfy "strong absorbing capacity, wide efficient absorbing bandwidth (EAB), thin matching thickness, and low density" [7,8].

Carbon has been extensively investigated and considered as a research concern as MA material due to its good stability, low density, and diverse morphological characteristics. Examples include zero-dimensional (0D) carbon quantum dots [9], 1D carbon nanotubes [10,

11], 2D graphene [12–14], 3D carbon spheres [15], and carbon composite materials [16,17]. In particular, carbon spheres and nanocubes possess the best plasticity and mesoporous morphology, which is conducive to impedance mismatching and reflection of electromagnetic waves. Zhang et al. [18] fabricated and applied hollow carbon microspheres with adjustable mesopores. The unique structure provided scattering and multi-reflection inside the absorbers, leading to favorable MA performance with the minimum reflection loss (RL$_{min}$) of −30.4 dB at thickness of 3.6 mm. Chen et al. [19] fabricated Fe@NCNs (N-doped carbon nanocubes)/MnO$_2$ yolk-double shell materials and investigated the heterogeneous interface resulting from phase separation and the mechanism of MA properties of the absorbers. The results showed that the RL$_{min}$ of −46.7 dB was achieved at 3.3 mm, and the EAB reached 10.8 GHz at 3.1 mm thickness. Magnetic materials are considered as one of the most widely studied MA materials. The excellent magnetism provides magnetic loss, and magnetic materials can be combined with dielectric and conductive materials to achieve synergistic effect

[20–22]. As a spinel-type transition metal oxide, CoFe₂O₄ exhibits superior magnetic loss performance with certain dielectric loss, thereby it is widely used in the synthesis of MA materials. For example, Cheng et al. [23] applied a biomimetic layered absorber composed of carbon and CoFe₂O₄ with RL$_{min}$ value reaching −53.54 dB at 2.46 mm, and maximum EAB reached 4.92 GHz at 1.7 mm. The excellent absorbing performances are attributed to the combined action of dielectric loss, conductive loss, and magnetic loss, resulting in the synergistic effect of hollow structure and interface effect. MA materials with a single structure and component generally possess poor impedance matching, narrow absorbing bandwidth, and low reflection loss. In general, MA materials with the yolk-shell structure are effective for optimizing the impedance matching and increasing the multiple reflections responsible for absorbing electromagnetic waves. Moreover, the interfacial relaxation of yolk-shell structure resulting from hetero-interfaces-induced polarization has been proven to be conducive to enhancing the absorbing performance [24]. Examples of such materials include Fe/m-SiO₂/PPy [25], Co@SiO₂@C [26], air@Co@Co₃Sn₂@SnO₂ [27], and C@void@C [28]. However, despite the extensive research efforts devoted to the study on the yolk-shell materials, most research has been focused on the overall impedance matching through internal and external synergism; nonetheless, the effect of impedance matching between the outer shell and free space has not been thoroughly investigated. The doping of nonmetallic atoms in carbon has been shown to improve impedance matching. For instance, Jiang et al. [29] reported S-NCFs (S/N atoms-doped carbon nanofibers) with massive number of dipoles to improve the dipole polarization effect of the absorber and thus optimized its impedance matching performance. The resulting S-NCFs exhibited the RL$_{min}$ value of as low as −48.67 dB at 16.1 GHz, while the thickness was 1.39 mm with a mass ratio of 15%. The doping of heteroatoms based on carbon helps in designing particular yolk-shell structure absorbers with complete impedance matching, feasible for optimizing the impedance matching performance of yolk-shell materials.

In this study, an N-doped honeycomb carbon shell with a CoFe₂O₄ core was synthesized by solvothermal method followed by hydrolysis, etching, and annealing. The resulting composite materials combined the advantages of magnetic materials and carbon materials to provide various absorbing mechanisms. The abundant honeycomb pores and voids between the core and shell generated an enormous amount of reflection space and specific surface area, allowing multiple reflections of electromagnetic waves and improved absorbing efficiency. The doping of N atoms reduced the electrical conductivity, introduced dipoles and defects, and improved the impedance matching on the microsphere surface. This, in turn, declined the immediate reflection of microwave incidents on the surface. The electromagnetic properties of the resulting yolk-shell structure absorbers were thoroughly discussed along with the MA mechanism of synthetic samples. Overall, these findings provide new insights into the impedance matching design of MA materials with yolk-shell structure, relevant for future uses.

2. Experimental

2.1. Materials

Cobalt(II) chloride hexahydrate (CoCl₂·6H₂O) was purchased from Xilong Scientific. Iron chloride hexahydrate (FeCl₃·6H₂O, 99.0%) and tetrapropyl orthosilicate (TPOS, 97%) were obtained from Aladdin. Resorcinol (C₆H₆O₂, 99%), formaldehyde solution (CH₂O, 37.0 wt%), and polyethylene glycol 2000 (PEG 2000) were received from Macklin. Melamine (C₃H₆N₆, 99%), ammonia solution (NH₃·H₂O, 25.0 wt%), ethylene glycol (EG, 98%), urea (CH₄N₂O, 99%), and sodium hydroxide (NaOH, 97%) were all provided by Sinopharm. All chemicals were of AR grade and used as received without any further purification. Deionized water was prepared in our laboratory using an ultrapure water machine.

2.2. Preparation of CoFe₂O₄ nanospheres

CoFe₂O₄ nanospheres were synthesized by the hydrothermal process. Typically, CoCl₂·6H₂O (928.65 mg), FeCl₃·6H₂O (1688.25 mg), PEG-2000 (1000 mg), and urea (2800 mg) were dispersed in EG (80 mL) under magnetic stirring for 2 h. Next, the solution was transferred into a 150-mL Teflon reactor and heated in an oven at 190 °C for 12 h. After cooling down to room temperature, the resulting black powders were cleaned with deionized water and absolute ethanol three times, which was followed by drying under vacuum at 45 °C for 20 h to yield CoFe₂O₄ microspheres.

2.3. Preparation of CoFe₂O₄@Resorcinol–Formaldehyde (RF)/SiO₂ nanospheres

First, the as-prepared CoFe₂O₄ nanospheres (200 mg) were dispersed in mixed deionized water (80 mL) and absolute ethanol (15 mL) solution. The resulting mixture was then ultrasonically dispersed to separate for 10 min followed by mechanical agitation. Next, NH₃·H₂O (3 mL) and TPOS (1.5 mL) were added into the mixture and the contents were kept stirring for 2 min. Then, formaldehyde solution (0.7 mL) and resorcinol (500 mg) were added dropwise into the mixture followed by stirring for 24 h at 30 °C. The obtained mixture was then dried under vacuum at 60 °C for 12 h to obtain CoFe₂O₄@RF/SiO₂ microspheres.

2.4. Preparation of CoFe₂O₄@HC nanospheres

The collected CoFe₂O₄@RF/SiO₂ microspheres were fully ground followed by carbonization in a tube furnace containing Ar at 700 °C (5 °C·min⁻¹) for 2 h to yield CoFe₂O₄@C/SiO₂. The honeycomb structure was obtained by etching the reaction. To this end, CoFe₂O₄@C/SiO₂ microspheres were dispersed in a solution of NaOH (1 M, 100 mL) and left under mechanical stirring for 24 h to remove SiO₂. The resulting product was then cleaned with deionized water and absolute ethanol three times to yield CoFe₂O₄@HC after drying in vacuum at 60 °C for 12 h. The honeycomb carbon shell (HC) was synthesized following the same procedure mentioned above, but without using CoFe₂O₄ as a core.

2.5. Preparation of CoFe₂O₄@HCN nanospheres

CoFe₂O₄@HC microspheres were ground and mixed thoroughly with melamine at a mass ratio of 2:3. Then, the mixed powders were heat treated under N₂ at 700 °C (5 °C·min⁻¹) for 2 h, and the final product was obtained by magnetic separation.

2.6. Characterization

Crystalline structures and phase compositions were analyzed by X-ray diffraction (XRD, Bruker, D8 Advance) with CuKα radiation and λ = 1.5406 Å. The morphologies and particle sizes were characterized by scanning electron microscopy (SEM, Hitachi SU8010, including energy-dispersive spectroscopy (EDS). The surface components and chemical bonds were examined by X-ray photoelectron spectroscopy (XPS, Escalab-250 X-ray). The Raman spectra were obtained using a Raman spectrometer (alpha-300R, Witec) at a laser excitation of 532 nm. Fourier transform infrared (FT-IR) spectrometer were measured by Thermo Scientific Nicolet iS20. The Brunauer–Emmett–Teller (BET) surface area was measured using a TriStar II 3020, Micromeritics Instrument Corporation. Barret–Joyner–Halenda (BJH) pore size distribution was calculated from the absorption isotherms by using the nonlocal density functional theory. The magnetic properties were obtained using a magnetic measurement system (VSM, Lakeshore7407).

2.7. Electromagnetic parameters measurement

Before measurements, the samples were ground into fine powders

followed by mixing with paraffin with a mass ratio (40 wt% for samples, 60 wt% for paraffin) before pressing through a specific mold into a co-axial ring with an outer diameter of 6.95 mm and inner diameter of 3.05 mm. The complex permittivity ($\varepsilon_r = \varepsilon' - j\varepsilon''$) and permeability ($\mu_r = \mu' - j\mu''$) of each composite were evaluated using a vector network analyzer (VNA, Agilent N5244A) in the range of 2–18 GHz.

3. Results and discussion

The fabrication process of CoFe$_2$O$_4$@HCN yolk-shell microspheres is shown in Fig. 1. First, CoFe$_2$O$_4$ microspheres were formed spontaneously from Fe^{3+} and Co^{2+} in solution by the hydrothermal reaction. Second, CoFe$_2$O$_4$ was used as the core to allow the hydrolysis of TPOS and polymerization of RF for the simultaneous formation of the interlaced structure. Third, the RF was decomposed into carbon by annealing, and SiO$_2$ was subsequently etched with NaOH to obtain CoFe$_2$O$_4$@HC. Finally, CoFe$_2$O$_4$@HCN was obtained by annealing CoFe$_2$O$_4$@HC and melamine mixture under N$_2$.

Fig. 2a shows the SEM image of CoFe$_2$O$_4$ microspheres. Obviously, CoFe$_2$O$_4$ particles displayed a spherical shape with irregular grooves and pores (diameters around 230–310 nm). Such structure is expected to be helpful in enhancing the multi-reflection and absorption of microwaves. Fig. 2b exhibits the morphology of the as-prepared honeycomb porous carbon shells, illustrating a regular spherical shape with clear nanoscale cellular pores. Fig. 2c demonstrates that CoFe$_2$O$_4$@HC microspheres exhibited HC with regular shell shape uniformly coated on CoFe$_2$O$_4$ core. The top right of Fig. 2c also shows a bare CoFe$_2$O$_4$ core maintaining the same morphology similar to the original CoFe$_2$O$_4$ microspheres, with the thickness of the HC shell of 65 nm being independent of the core diameter. Therefore, the coating of the honeycomb carbon shell and annealing barely affected the morphology of the CoFe$_2$O$_4$ core. The morphology of CoFe$_2$O$_4$@HCN shown in Fig. 2d reveals that the doping of N atoms did not affect the porosity and structure of the HC shell. The HC/HCN shell consisted of numerous honeycomb pores structures, introducing interface and reflective cavity. The unique yolk-shell structure and multi-reflective interface were critical to the attenuation of microwave energy. The EDS element mapping of CoFe$_2$O$_4$@HCN shown in Fig. 2e confirms the presence of N with the same distribution of C, indicating the successful doping of the N atoms into the material microsphere. Overall, the yolk-shell structure with numerous honeycomb pores was successfully synthesized.

Typical XRD patterns of HC, CoFe$_2$O$_4$, CoFe$_2$O$_4$@HC, and CoFe$_2$O$_4$@HCN are presented in Fig. 3a. All samples associated with CoFe$_2$O$_4$ showed peaks perfectly corresponding to PDF#22–1086 (CoFe$_2$O$_4$). The diffraction peaks at 2θ values of 18.29°, 30.08°, 35.43°, 43.06°, 56.94°, and 62.53° were indexed to (111), (220), (311), (400), (511), and (440) crystal planes of CoFe$_2$O$_4$(PDF#22–1086), respectively. The CoFe$_2$O$_4$, CoFe$_2$O$_4$@HC, and CoFe$_2$O$_4$@HCN samples exhibited high crystallinity, indicating that the honeycomb carbon shell and annealing did not affect the core crystal structure. The XRD pattern of HC revealed a broad peak at 19°–23°, indicating the presence of the amorphous carbon [30], as confirmed by the XRD patterns of CoFe$_2$O$_4$@HC and CoFe$_2$O$_4$@HCN, revealing the successful coating of HC and HCN on CoFe$_2$O$_4$ microspheres.

The Raman spectra of CoFe$_2$O$_4$@HC and CoFe$_2$O$_4$@HCN are shown in Fig. 3b. The peak at 1350 cm^{-1} is attributed to the disordered vibrations at the boundary of the hexagonal Brillouin zone, expressing the level of defects in the lattice of carbon atoms. The peak at 1590 cm^{-1} is attributed to the stretching vibration mode of the in-plane bond of C atoms related to the graphitization degree [31,32]. The defect density of a material can be expressed by the value of the intensity ratio of peaks (I_D/I_G). The calculated I_D/I_G values of CoFe$_2$O$_4$@HC and CoFe$_2$O$_4$@HCN are 0.9474 and 0.9704, respectively. The elevated I_D/I_G value after nitridation indicates an increase in defects of the carbon shell caused by the doping of N atoms and the production of N-containing functional groups. These defects and functional groups produced interfacial polarization and dipole polarization effects in the presence of the alternating electromagnetic field. Moreover, the multi-scattering among the defects may contribute to the loss capacity of electromagnetic waves [13].

The magnetic performances under alternating magnetic fields of the samples are provided in Fig. 3c. Noteworthy, the magnetization of CoFe$_2$O$_4$, CoFe$_2$O$_4$@HC, and CoFe$_2$O$_4$@HCN was measured by VSM under magnetic fields of −20,000 to 20,000 Oe at 25 °C. The presence of obvious long-narrow hysteresis loops indicates the existence of magnetic hysteresis loss. The absorbers showed strong ferromagnetic behaviors with *Ms* value of 72.94 emu·g^{-1} for CoFe$_2$O$_4$, while those of CoFe$_2$O$_4$@HC and CoFe$_2$O$_4$@HCN reduced to 62.40 and 65.48 emu·g^{-1}, respectively. The decrease in *Ms* value can be explained by the increase in the content of the non-magnetic components. Furthermore, the *Hc* values of CoFe$_2$O$_4$, CoFe$_2$O$_4$@HC, and CoFe$_2$O$_4$@HCN were estimated to be 93, 142, and 152 Oe, respectively (Fig. 3c). The increase in *Hc* values was attributed to the enhanced anisotropy caused by annealing [33]. In general, high initial magnetic permeability (μi) favors strong magnetic losses, and μi can be calculated according to Eq. (1) [34]:

$$\mu_i = \frac{M_s^2}{akH_cM_s + b\lambda\xi} \tag{1}$$

where *a* and *b* are two constants determined by the composition of materials, λ refers to the magnetostriction constant, and ξ denotes the elastic strain parameter of the material. Notably, higher *Ms* and lower *Hc* induce higher μ_i, conducive to promoting stronger magnetic loss.

The surface composition and chemical bond of CoFe$_2$O$_4$@HCN characterized by XPS are displayed in Fig. 3(d–f). The survey spectrum of CoFe$_2$O$_4$@HCN displayed a composite mainly containing C, N, O, Fe, and Co elements (Fig. 3d). The absence of Co and Fe signals was probably caused by the effective detection depth of XPS, which did not surpass 10 nm, thereby becoming incapable of penetrating the honeycomb carbon shell with thickness of 60 nm [35]. The high-resolution spectrum of C 1s shown in Fig. 3e can be deconvoluted into four peaks ascribed to the C–C/C≡C group (284.80 eV), C–N group (285.82 eV), C–O group (286.72 eV), and O–C≡O group (289.06 eV) [4,8]. Fig. 3f exhibits that the high-resolution N 1s spectrum can be deconvoluted into four peaks, attributed to pyridinic N (398.57 eV), pyrrolic N (399.87 eV), graphitic N (400.97 eV), and oxidized N (403.29 eV), respectively [36,37]. This supported the EDS data and confirmed the successful incorporation of N atoms into the honeycomb carbon shell. The N atoms with different electronegativities than C atoms generated the dipole moments. The deflection of dipole moment under alternating electromagnetic field benefited the loss in electromagnetic waves.
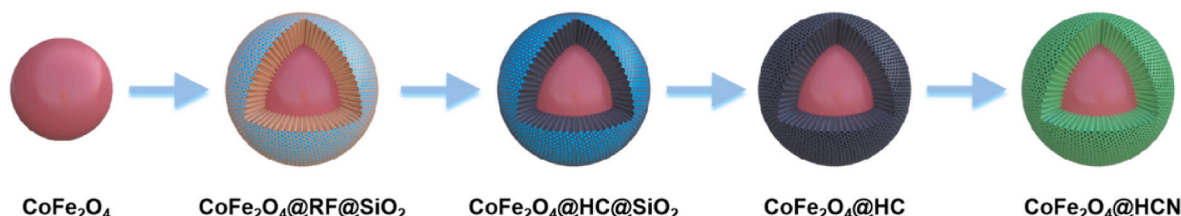

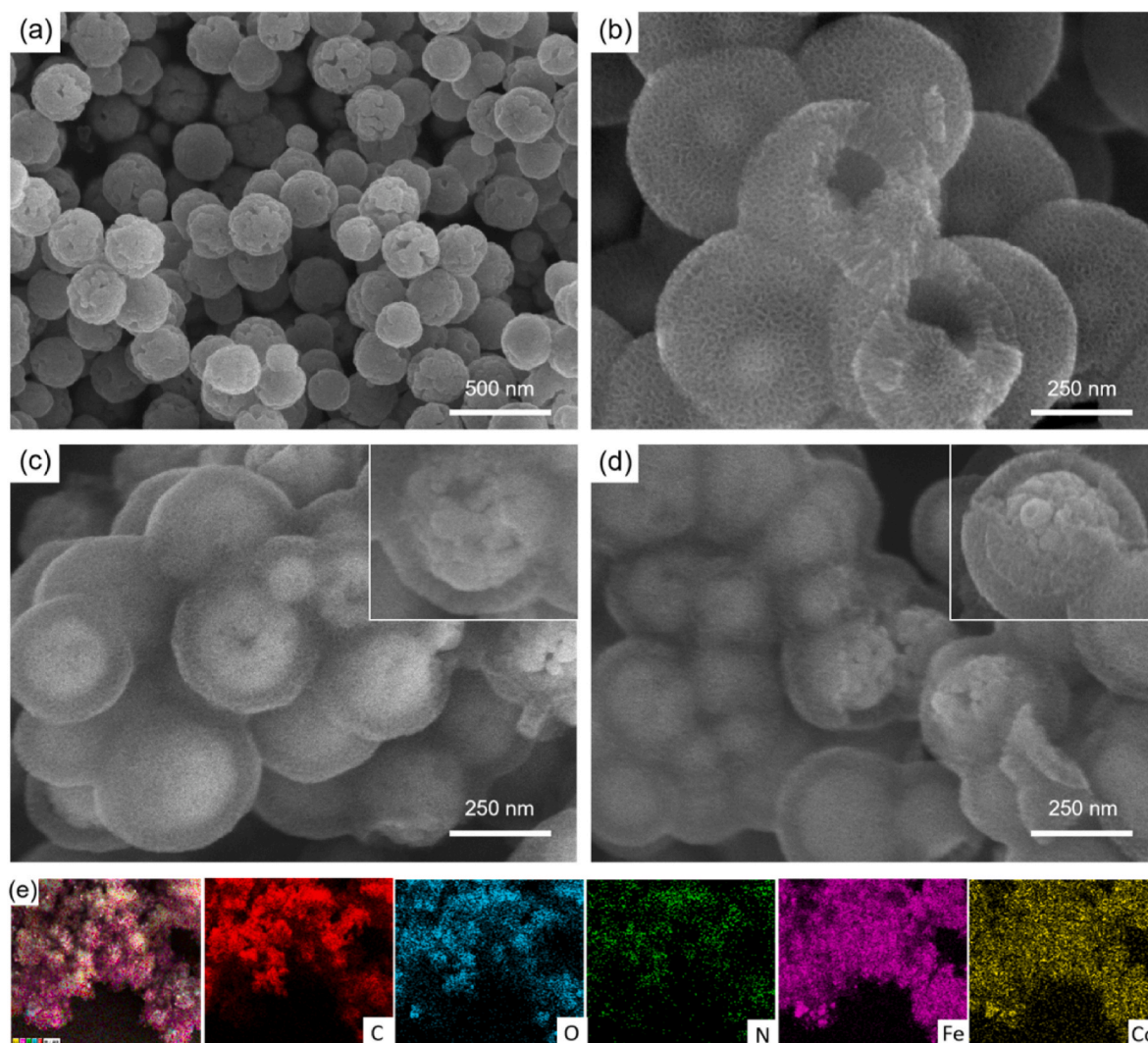**Fig. 1.** The preparation process of CoFe$_2$O$_4$@HCN microspheres.

Fig. 2. SEM images of (a) CoFe$_2$O$_4$, (b) HC, (c) CoFe$_2$O$_4$@HC, (d) and CoFe$_2$O$_4$@HCN. (e) EDS mapping of CoFe$_2$O$_4$@HCN.

Fig. S1 displays the Fourier transform infrared (FTIR) spectrum of CoFe$_2$O$_4$@HCN. The absorption peaks at 1629, 1388, and 1063 cm^{-1} are attributed to the C=C stretching vibration, =C–H in-plane vibration, and deformation vibrations of C–H, respectively [20,22]. The peak at 1459 cm^{-1} represents conjugated C–N stretching [22,38]. The peak appearing at 601 cm^{-1} is associated with Fe–O [39], indicating the existence of CoFe$_2$O$_4$. The FTIR spectroscopy result shows the consistency with the XRD and XPS results.

The microporous morphologies of the materials were analyzed by N$_2$ adsorption isotherms. The N$_2$ sorption isotherms and BJH pore size distributions of HC, CoFe$_2$O$_4$@HC, and CoFe$_2$O$_4$@HCN are presented in Fig. 4. All three materials exhibited type IV isotherms, indicating characteristics mesoporous morphologies [26,40]. The adsorption capacities of HC increased sharply in the low-pressure region (P/P$_0$ < 0.1), indicating the presence of a microporous structure corresponding to the smaller diameter pores located in the inner wall. HC showed an H4-type hysteresis loop at P/P$_0$ of 0.4–1.0 caused by the capillary condensation phenomenon, revealing the presence of layered honeycomb holes in the materials and corroborating the SEM data. Fig. 4(b and c) illustrate that both CoFe$_2$O$_4$@HC and CoFe$_2$O$_4$@HCN present a slow increase in adsorption capacity (P/P$_0$ < 0.1), which can be attributed to the blocking of the micropores by internal CoFe$_2$O$_4$ and partial destruction caused by annealing. CoFe$_2$O$_4$@HC and CoFe$_2$O$_4$@HCN revealed an H3-type hysteresis loop at P/P$_0$ of 0.4–1.0. The rapid increase in

adsorption at P/P$_0$ of 0.8–1.0 was contributed by the accumulation gap of particles. The surface grooves of CoFe$_2$O$_4$ nanospheres and voids between the nanospheres and carbon shells were responsible for the adsorption effect. In BJH model, the pore size of small holes can be characterized by dV/dlog(D). The BJH pore size distributions of HC shown in Fig. 4a reveal the presence of peaks at 2.3 nm, corresponding to the honeycomb mesopores of the carbon shell. The large pores at 52 nm in CoFe$_2$O$_4$@HC corresponded to the grooves in the CoFe$_2$O$_4$ cores and the gaps between the broken shells and cores (Fig. 4b). The macropore size of CoFe$_2$O$_4$@HCN further increased to 72 nm (Fig. 4c), consistent with the N$_2$ adsorption/desorption curves. For porous materials, the presence of mesopores and macropores provide numerous surfaces for the scatter and reflection of microwaves, contributing extremely to the MA properties of absorbers. The BET surface areas of HCN, CoFe$_2$O$_4$@HC, and CoFe$_2$O$_4$@HCN were 886.77, 677.17, and 592.27 m$^2 \cdot$g^{-1}, respectively. The decrease in the values of CoFe$_2$O$_4$@HC and CoFe$_2$O$_4$@HCN stemmed from the addition of CoFe$_2$O$_4$ core, thereby masking the internal pores. The annealing and oxidation also caused the collapse of some microporous structures. High BET surface areas and nanoscale pore size indicate the material with elevated porosity. The Maxwell Garnet equation model and air-to-material interface intrinsic reflection coefficient (Γ) can be calculated according to Eqs. (2) and (3) [41–43].:
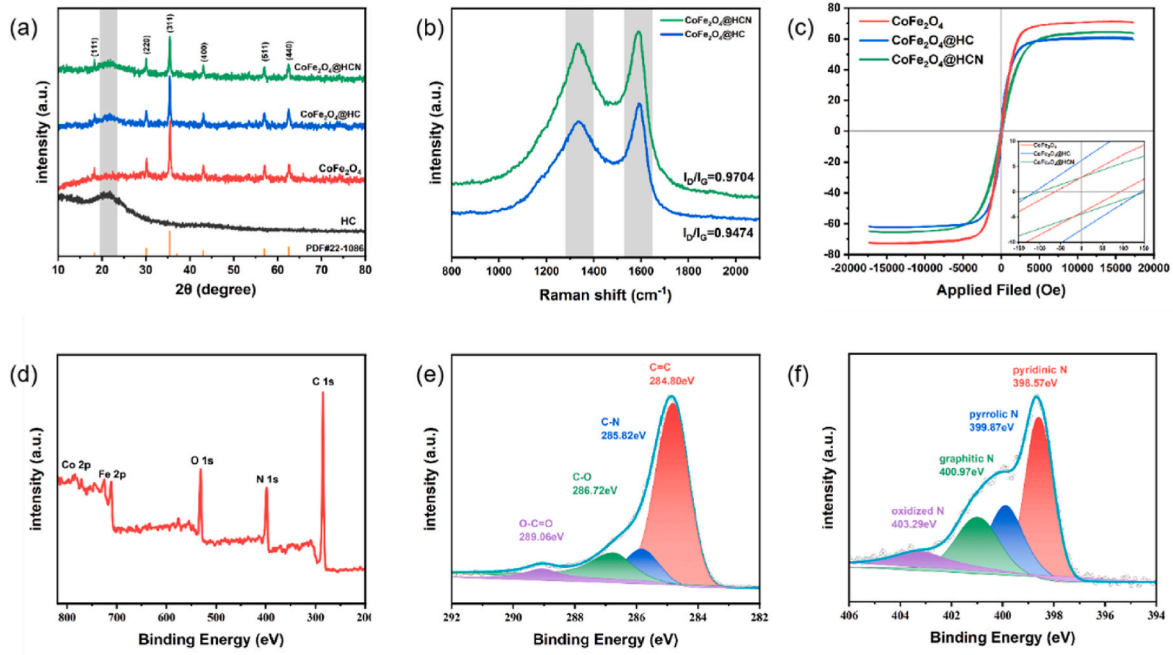
Fig. 3. (a) XRD patterns of HC, CoFe$_2$O$_4$, CoFe$_2$O$_4$@HC, and CoFe$_2$O$_4$@HCN. (b) Raman spectra of CoFe$_2$O$_4$@HC and CoFe$_2$O$_4$@HCN. (c) Magnetic hysteresis loops of CoFe$_2$O$_4$, CoFe$_2$O$_4$@HC, and CoFe$_2$O$_4$@HCN. XPS spectra of (d) survey spectrum, (e) C 1s, and (f) N 1s.
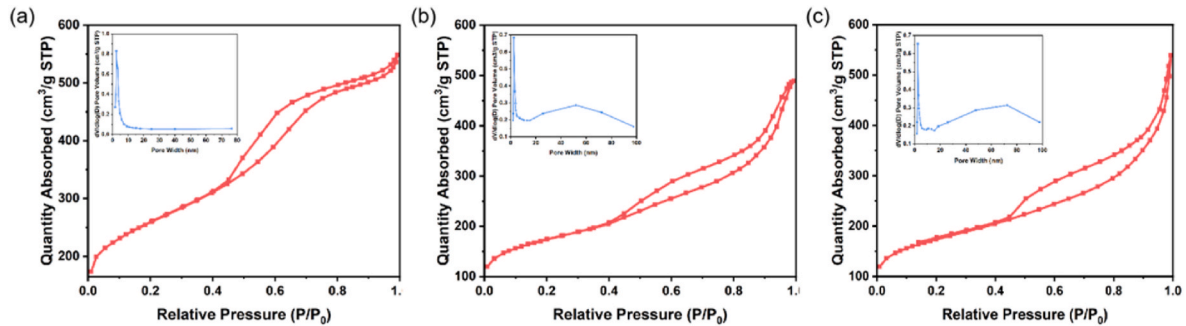

Fig. 4. N$_2$ adsorption–desorption isotherm and pore size distribution of (a) HC, (b) CoFe$_2$O$_4$@HC, and (c) CoFe$_2$O$_4$@HCN.

$$\varepsilon_{eff}^{MG} = \left[\frac{(2\varepsilon_1 + \varepsilon_2) + 2\nu(2\varepsilon_2 - \varepsilon_1)}{(2\varepsilon_1 + \varepsilon_2) - \nu(\varepsilon_2 - \varepsilon_1)} \right] \varepsilon_1 \qquad (2)$$

$$\Gamma = \frac{\sqrt{\frac{\mu_r}{\varepsilon_r}} - 1}{\sqrt{\frac{\mu_r}{\varepsilon_r}} + 1} \qquad (3)$$

where ν is the volume fraction of the pores. ε_1 and ε_2 represent the permittivity of matrix material and air in the pores. ε_r and μ_r represent the complex permittivity and complex permeability, respectively.

Large air volume facilitates the reduction of effective permittivity. For materials with low magnetic permeability, smaller permittivity values result in lower Γ, leading to the diminished reflection of the microwaves incident on the materials. Moreover, the honeycomb 3D carbon structure could also form conductive networks. According to the literature [44], electrons in electrons hopping mode could transfer in the yolk-shell structure consisting of CoFe$_2$O$_4$ and carbon by absorbing microwave energy to transform it into heat through dissipation.

To evaluate the MA properties, the reflection loss (RL) was calculated by using the transmission line theory [45,46]:

$$Z_{in} = Z_0 \sqrt{\mu_r/\varepsilon_r} \tan h \left[j(2\pi fd/c)\sqrt{\mu_r\varepsilon_r} \right] \qquad (4)$$

$$RL = 20 \log \left| (Z_{in} - Z_0)/(Z_{in} + Z_0) \right| \qquad (5)$$

where Z_{in} is the input characteristic impedance of the materials, Z_0 represents the impedance of free space, c refers to the velocity of light in vacuum, and d is the thickness of material.

The 3D diagrams and corresponding contour diagrams of the RL values of HC, CoFe$_2$O$_4$, CoFe$_2$O$_4$@HC, and CoFe$_2$O$_4$@HCN at frequencies within 2–18 GHz and d values of 1–5.5 mm are provided in Fig. 5. In general, RL below −10 dB indicates that absorbing rates of electromagnetic waves reach 90%, while RL below 20 dB refers to absorbing rates reaching 99%. Furthermore, absorbers with an RL of −10 dB or less possess practical application capability [47]. Fig. 5a illustrates that the hollow HC exhibits low reflection loss characteristics with RL$_{min}$ value of −20.57 dB at 10.96 GHz for a thickness of 2.5 mm and the EAB is 3.56 GHz (9.28–12.84 GHz). For bare CoFe$_2$O$_4$ microspheres (Fig. 5b), the RL$_{min}$ at the thickness of 5.0 mm reached −17.51 dB at 6.12 GHz and EAB reached 2.52 GHz (4.92–7.44 GHz). Therefore, RL$_{min}$, EAB, and thickness of both materials were not sufficient for practical application. Such poor MA properties were consistent with their monotonic composition and structure. In contrast, the materials after the composite formation exhibited excellent MA properties. Fig. 5c
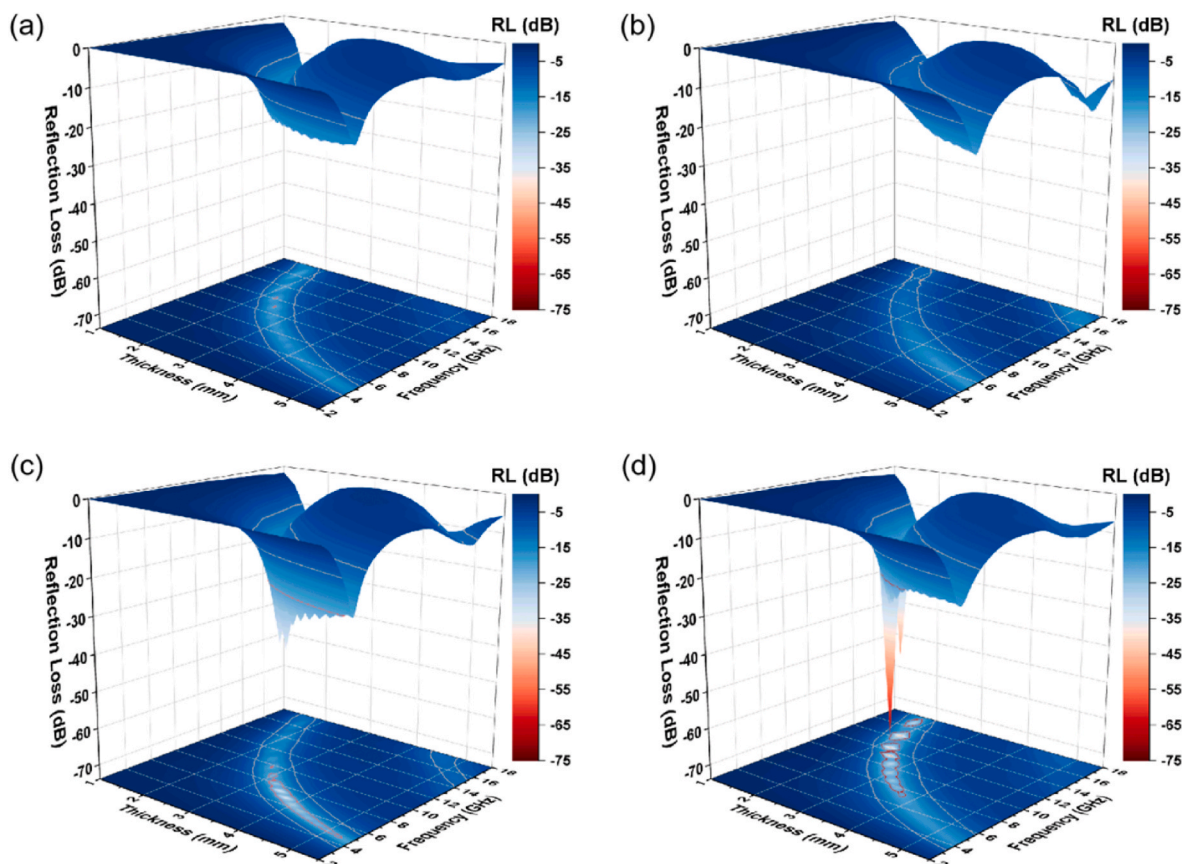
Fig. 5. Three-dimensional reflection loss of (a) HC, (b) $CoFe_2O_4$, (c) $CoFe_2O_4@HC$, and (d) $CoFe_2O_4@HCN$.

demonstrates that the RL_{min} value of $CoFe_2O_4@HC$ at d of 3.5 mm reached −34.49 dB at 7.32 GHz, while EAB reached 2.96 GHz (from 5.96 to 8.92 GHz). The absorber exhibits useable absorbing properties at 2–5 mm. In comparison, the other RL_{min} values were much lower than −10 dB. Thus, the unique structure formed by $CoFe_2O_4$ and HC and synergistic effect of magnetic and conductive properties achieved decent MA properties. Among all four samples, $CoFe_2O_4@HCN$ (Fig. 5d) illustrated the most desirable characteristics suitable for applications as an excellent absorber. The RL_{min} value at 2.5 mm thickness reached −68.03 dB at 11.36 GHz, and the EAB was 4.52 GHz (from 9.4 to 13.92 GHz). Significantly, with the decrease in the thickness to 1.99 mm, the RL_{min} value still maintained −58.34 dB, while the EAB broadened to 5.92 GHz (from 11.92 to 17.84 GHz). Therefore, the doping of N atoms effectively improved the MA properties and thinned the matching thickness of the samples. The MA performance of typical yolk-shell absorbers with binary or more materials and absorbers with $CoFe_2O_4$ and carbon based are listed in Table 1. The results indicate that $CoFe_2O_4@HCN$ possesses a high reflection loss ability and wide EAB with lower thickness, in addition, $CoFe_2O_4@HCN$ owns a lighter density compared to extreme performance absorbers, resulting a superior applicability.

In general, the main factor determining the MA performance consists mainly of impedance matching ($|Z_{in}/Z_0|$) [48], where a value of $|Z_{in}/Z_0|$ closer to 1 represents a better impedance matching and lower proportion of reflection. The changes in curves of $|Z_{in}/Z_0|$ values versus frequency at different thicknesses are presented in Fig. 6. The $|Z_{in}/Z_0|$ values of HC and $CoFe_2O_4$ exhibit significant deflection from the dashed line ($|Z_{in}/Z_0| = 1$), as shown in Fig. 6a and b. For $CoFe_2O_4@HC$ (Fig. 6c), the $|Z_{in}/Z_0|$ value is close to the dashed line at 6.28 GHz with a thickness of 3.5 mm, which can be attributed to the combination of $CoFe_2O_4$ and HC. Fig. 6d exhibits that $CoFe_2O_4@HCN$ show two regions close to the dashed line at 11.36 GHz at 2.5 mm and 14.4 GHz at 1.99 mm. Thus, the introduction of N atoms led to significant optimization of the impedance

Table 1

Microwave absorption performance comparison of yolk-shell absorbers/ $CoFe_2O_4$ & carbon based absorbers in recent literature.

Absorbers	RL_{min} (dB)	EAB (GHZ)	Thickness (mm)	Refs.
$MnO_2@PANI$	−52.06	4.56	3.00	[55]
$Fe_3O_4@C@MnO_2$	−58.25	5.56	4.20	[65]
$Co_3Fe_7/FeO@C$	−57.60	5.27	2.50	[66]
$CIP@void@NC$	−25.70	6.90	1.70	[67]
$ZnFe_2O_4@PHCMS$	−51.43	3.52	4.80	[68]
NRGO/hollow $CoFe_2O_4$	−44.70	5.20	1.80	[69]
$rGO/SiC/CoFe_2O_4$	−65.49	2.30	1.06	[70]
$CoFe_2O_4/MWCNTs$	−50.80	<3.36	4.20	[71]
$CoFe_2O_4$, (Fe, Ni) and carbon frame	−34.30	<6.55	2.00	[72]
$CNTs@CoFe_2O_4/polyimide$	−54.40	6.70	2.60	[73]
porous carbon@$CoFe_2O_4$	−67.04	5.52	2.00	[74]
$CoFe_2O_4@HCN$	−68.03	4.52	2.50	This work
	−58.34	5.92	1.99	This work

matching performance of the outer layer of the absorber, indicating that the microwave's reflection would be rare at the first moment of incidence at the surface.

Since thickness exhibits an obvious influence on the MA process, the relationship between RL and thickness was investigated as a function of frequency. Fig. 6 depicts that the RL_{min} peaks shifted toward the low-frequency region with the increase in the thickness of the materials, which is explained by the 1/4 wavelength matching model. The matching thickness (t_m) and peak frequency (f_m) satisfy the following relationship [49–51]:
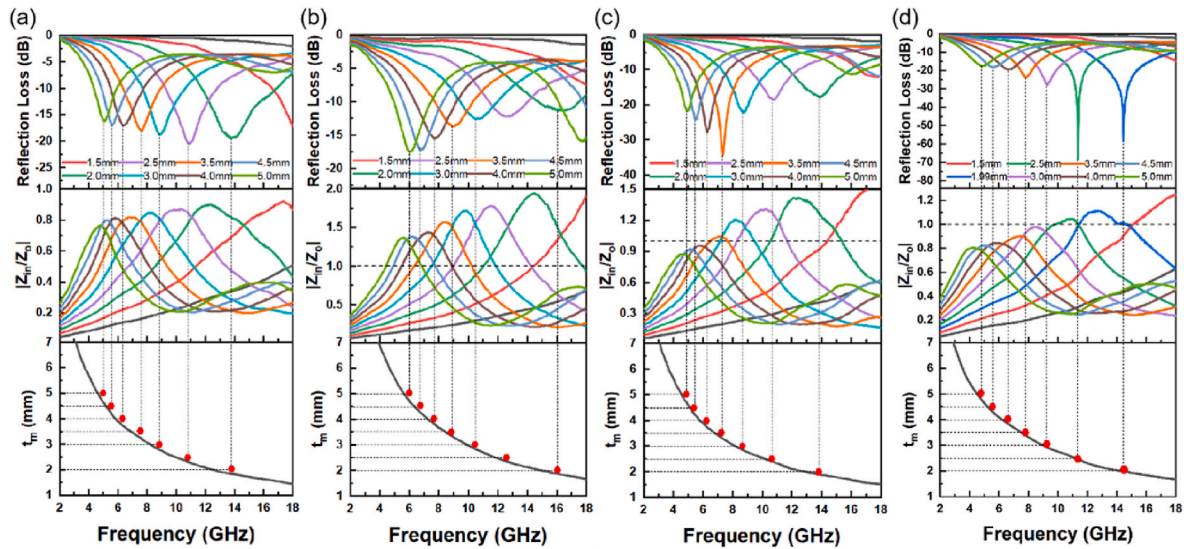
Fig. 6. Stack plots of two-dimensional reflection loss, impedance matching ($|Z_{in}/Z_0|$), and matching thickness (t_m) versus frequency for (a) HC, (b) CoFe$_2$O$_4$, (c) CoFe$_2$O$_4$@HC, and (d) CoFe$_2$O$_4$@HCN.

$$t_m = \frac{n\lambda}{4} = \frac{nc}{4f_m\sqrt{|\varepsilon_r||\mu_r|}} \quad (n = 1, 3, 5 \cdots) \tag{6}$$

Notably, for an absorber conforming to the 1/4 wavelength matching model, the reflected electromagnetic waves from the interface lag the incident wave by 180°, resulting in a strong interference effect leading to high RL_{min} values [29,52]. Fig. 6 exhibits that the experimental matching thicknesses of all samples highly matched the theoretically calculated values, confirming absorbers obeying the 1/4 wavelength model.

In order to further analyze the MA mechanism of the as-prepared samples, the ε', ε'', μ', and μ'' of HC, CoFe$_2$O$_4$, CoFe$_2$O$_4$@HC, and CoFe$_2$O$_4$@HCN were obtained between 2 and 18 GHz (Fig. 7). Herein, the ε' and ε'' represent the storage capacity and loss capacity of electric energy, respectively, while μ' and μ'' refer to the storage capacity and

loss capacity of magnetic energy, respectively. The variations in ε' of all samples versus frequency are provided in Fig. 7a. Obviously, the ε' values of three samples containing HC are higher than those of pure CoFe$_2$O$_4$ due to the electrical conductivity of HC. The ε' values of CoFe$_2$O$_4$@HC and CoFe$_2$O$_4$@HCN reduced when weakly conducting components were added. For CoFe$_2$O$_4$@HCN, the doping of N atoms restrained the conductivity of the carbon shell, resulting in a lower ε' when compared to CoFe$_2$O$_4$@HC [18], and lower ε' was found to be conducive to improving the dielectric loss tangent ($\tan\delta_\varepsilon$). The ε'' values versus frequency are presented in Fig. 7b. The ε'' can be drawn according to Eq. (7) [18]:

$$\varepsilon'' = \varepsilon_r'' + \varepsilon_c'' = \frac{\varepsilon_s - \varepsilon_\infty}{1 + \omega^2\tau^2} + \frac{\sigma}{\omega\varepsilon_0} \tag{7}$$

where ε_r'' and ε_c'', successively, represent the polarization loss and
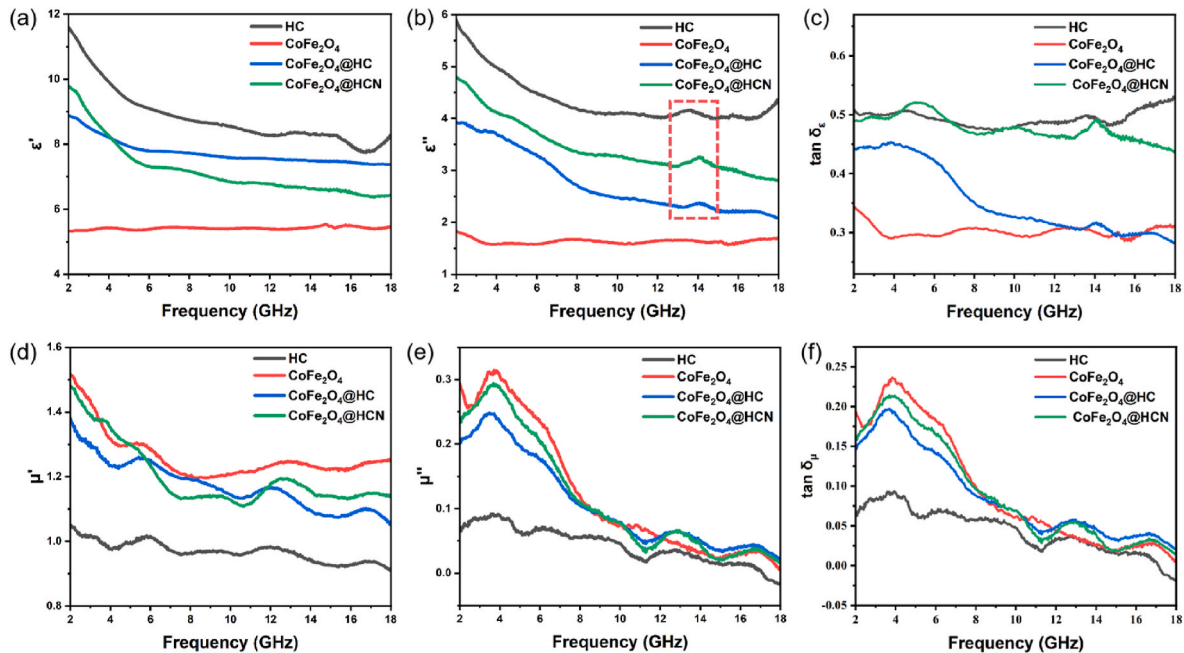

Fig. 7. (a) Real part of permittivity, (b) imaginary part of permittivity, (c) dielectric loss tangents $\tan\delta_\varepsilon$, (d) real part of permeability, (e) imaginary part of permeability, and (f) magnetic loss tangents $\tan\delta_\mu$ of HC, CoFe$_2$O$_4$, CoFe$_2$O$_4$@HC, and CoFe$_2$O$_4$@HCN.

conductive loss, while ε_s, ε_∞, σ, and τ correspond to the static dielectric constant, dielectric constant at infinite frequency, electrical conductivity, and polarization relaxation time, respectively [53,54].

The ε'' of HC seemed to be relatively large due to the highest electrical conductivity. CoFe$_2$O$_4$@HC led to the decrease in ε'' due to the addition of insulating CoFe$_2$O$_4$. Noteworthy, after doping with N atoms, the ε'' of CoFe$_2$O$_4$@HCN significantly increased when compared to CoFe$_2$O$_4$@HC owing to the stronger polarization loss performance, in particular, for dipole polarization generated by C–N dipoles. All three materials containing similar carbon shells showed a frequency relaxation resonance peak at 13–14 GHz associated with the interface polarization effect of honeycomb carbon shells [55,56]. Usually, tanδ_ε (tan$\delta_\varepsilon := \varepsilon''/\varepsilon'$) is used to evaluate the dielectric loss capacity of the absorber. The tan δ_ε of HC and CoFe$_2$O$_4$@HCN was much larger than those of CoFe$_2$O$_4$@HC and CoFe$_2$O$_4$. The high ε_r of HC was not conducive to the impedance matching, while CoFe$_2$O$_4$@HCN achieved optimal dielectric properties due to the lower ε' and synergistic effect issued from conductive loss, interfacial polarization loss, and dipole polarization loss.

The mechanism of dielectric loss expressed by Debye polarization relaxation is divided into electron polarization, interface polarization, ion polarization, and dipole polarization. At high frequencies, current research exhibits the occurrence of both ion polarization and electron polarization. The interface polarization and dipole polarization are the main polarization mechanisms at 2–18 GHz. The Debye relaxation theory can be described by using Eq. (8) [57–59]:

$$\left(\varepsilon' - \frac{\varepsilon_s + \varepsilon_\infty}{2}\right)^2 + (\varepsilon'')^2 = \left(\frac{\varepsilon_s - \varepsilon_\infty}{2}\right)^2 \tag{8}$$
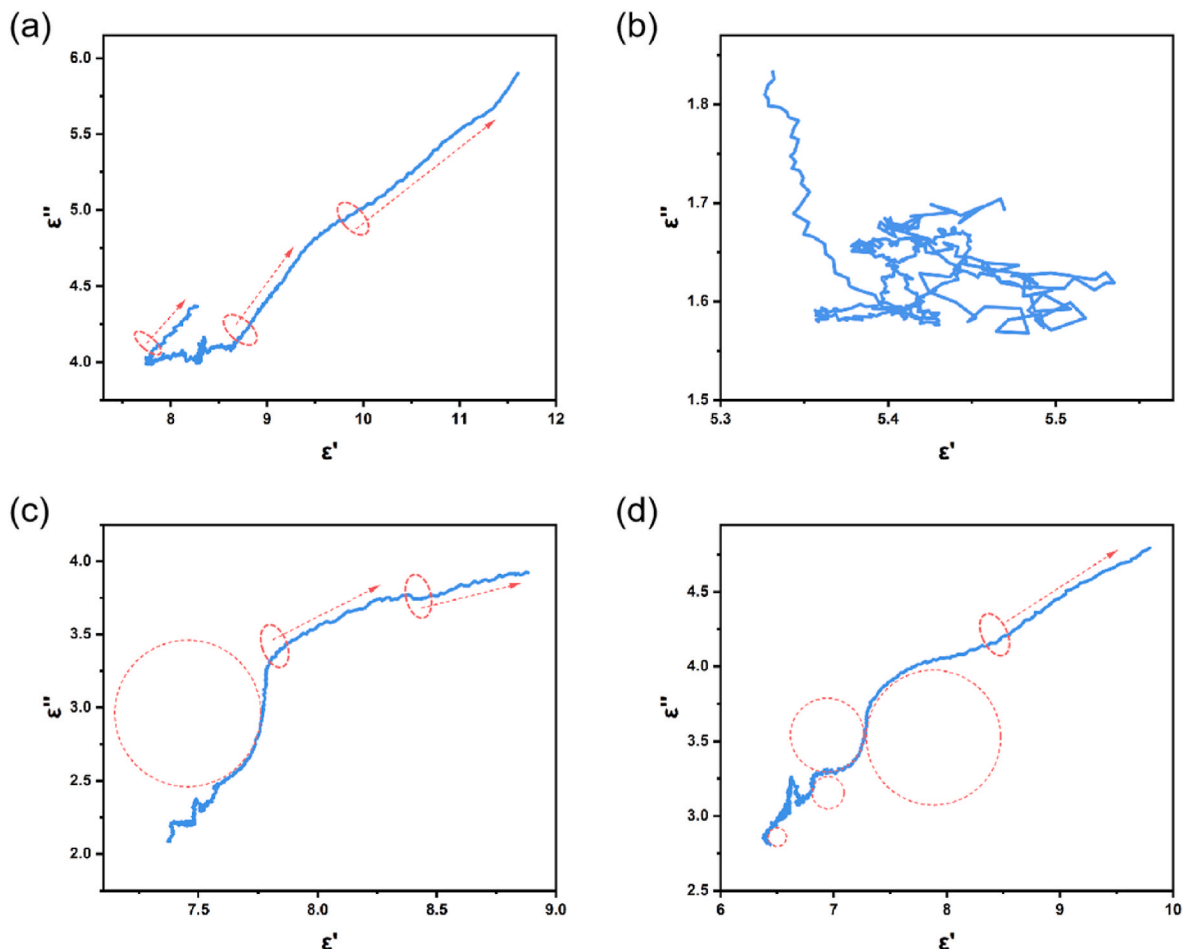
The semicircle relationship between ε' and ε'' (Cole–Cole semicircle) represents a Debye relaxation process. According to the previous study [11], the conductive loss replaces the dielectric loss as the main loss mechanism for $\varepsilon'–\varepsilon''$ curve showing a straight line [52,60]. The $\varepsilon'–\varepsilon''$ curves of HC, CoFe$_2$O$_4$, CoFe$_2$O$_4$@HC, and CoFe$_2$O$_4$@HCN are presented in Fig. 8. HC presented three-part linear relationship curves in Fig. 8a, indicating that loss capacity was mainly caused by conductive loss issued from the excellent electrical conductivity and 3D conductive network. Fig. 8b exhibits the presence of a completely disordered curve, indicating no conductive loss or dielectric loss in CoFe$_2$O$_4$. Fig. 8c presents that CoFe$_2$O$_4$@HC displayed one Cole–Cole semicircle and two-part linear relationship curves. The Cole–Cole semicircle corresponded to the Debye relaxation process caused by the heterogeneous interface of CoFe$_2$O$_4$ and HC. The heterogeneous aggregation of local charges around the interface formed interfacial polarization under the alternating electromagnetic field [26]. For CoFe$_2$O$_4$@HCN, four semicircles and one linear part were observed (Fig. 8d), indicating the occurrence of conductive loss and multi-relaxation processes such as interfacial polarization and dipole polarization. The natural dipole moment formed by C atoms and N atoms rearranged and oriented along the direction of the electric field under the action of the alternating electric field by absorbing electromagnetic energy [29].

The changes in μ' values as a function of frequency are presented in Fig. 7d. Noteworthy, the change is theoretically related to the proportion of magnetic components. The μ' values versus frequency of CoFe$_2$O$_4$, CoFe$_2$O$_4$@HC, and CoFe$_2$O$_4$@HCN fluctuated between 1.1 and 1.4, while the μ' of HC was below 1.0. The samples CoFe$_2$O$_4$, CoFe$_2$O$_4$@HC, and CoFe$_2$O$_4$@HCN showed high μ'' values than HC, as presented in Fig. 7e. The μ'' of CoFe$_2$O$_4$ was the highest in the range of

Fig. 8. Cole–Cole semicircles ($\varepsilon'–\varepsilon''$ curves) of (a) HC, (b) CoFe$_2$O$_4$, (c) CoFe$_2$O$_4$@HC, and (d) CoFe$_2$O$_4$@HCN.

2–8 GHz, while that of CoFe$_2$O$_4$@HCN was slightly lower than that of CoFe$_2$O$_4$ but slightly higher than that of CoFe$_2$O$_4$@HC. This may be related to the annealing process, which induced changes in Ms and Hc of CoFe$_2$O$_4$ core. Consequently, the μ'' curves of CoFe$_2$O$_4$, CoFe$_2$O$_4$@HC, and CoFe$_2$O$_4$@HCN almost overlapped in the region of 8–18 GHz. The magnetic loss capacity was evaluated by tanδ_μ (tan$\delta_\mu = \mu''/\mu'$), and the frequency-dependent tan δ_μ of as-prepared samples are provided in Fig. 7f. The trend of the tan δ_μ curves was almost the same as that of μ'' curves as a function of frequency. Samples containing CoFe$_2$O$_4$ displayed a higher magnetic loss than pure HC.

The mechanism of magnetic loss for the absorber can mainly be segmented into eddy current loss, domain-wall resonance, natural resonance, and magnetic hysteresis loss [53]. The domain-wall resonance of materials appeared only at the frequency of 1–100 MHz [61]. The natural resonance effect can be calculated by using Eqs. 9–11 [49, 62]:

$$K = \mu_0 M_s H_c / 2 \tag{9}$$

$$H_\alpha = 4|K|/3\mu_0 M_s \tag{10}$$

$$2\pi f_r = r H_\alpha \tag{11}$$

where K represents anisotropy coefficient, μ_0 represents the permeability of vacuum, H_α is the anisotropy energy, f_r denotes the resonant frequency, and r is the gyromagnetic ratio.

Herein, the resonant frequency depends on the anisotropy of the material mainly manifested by H_c. Fig. 3c exhibits that the H_c values of CoFe$_2$O$_4$@HC and CoFe$_2$O$_4$@HCN were larger than that of pure CoFe$_2$O$_4$, owing to the high natural resonance properties. The curve enclosed with a certain area by the hysteresis lines during magnetization indicates the existence of hysteresis loss. The eddy current loss coefficient could be described by using Eq. (12) [59,63]:

$$C_o = \mu''(\mu')^{-2}f^{-1} = 2\pi\mu_0 d^2\delta \tag{12}$$

where C_0 represents the eddy current loss coefficient, d is the diameter of the nanoparticle, and δ refers to the electrical conductivity.

The occurrence of eddy current loss in the absorber should result in a constant C_0 value versus frequency. The C_0 curves for HC, CoFe$_2$O$_4$, CoFe$_2$O$_4$@HC, and CoFe$_2$O$_4$@HCN shown in Fig. 9a reveal fluctuating C_0 values for all samples as a function of frequency, indicating minimal eddy current loss. Thus, the magnetic loss was mainly derived from natural resonance and magnetic hysteresis loss.

Attenuation constant (α) is used to evaluate the attenuation capacity of materials, and as a crucial parameter useful to determine the MA performance, which can be described in terms of Eq. (13) [64], as follows:

$$\alpha = \frac{\sqrt{2}\pi f}{c} \times \sqrt{(\mu''\varepsilon'' - \mu'\varepsilon') + \sqrt{(\mu''\varepsilon'' - \mu'\varepsilon')^2 + (\mu'\varepsilon'' + \mu''\varepsilon')^2}} \tag{13}$$

For impedance matching, higher α values should lead to stronger absorbing ability. The α values of four absorbers are provided in Fig. 9b. HC and CoFe$_2$O$_4$@HCN generated the highest loss abilities. For CoFe$_2$O$_4$@HCN, the high α values were issued from the synergistic effect contributed by conduction loss, dielectric loss, and magnetic loss.

Based on the above-mentioned analyses, a logical MA mechanism was constructed for CoFe$_2$O$_4$@HCN microspheres. In this mechanism, a strong ferromagnetic CoFe$_2$O$_4$ core provided ideal magnetic losses such as natural resonance and hysteresis losses. Numerous interfaces arising from the honeycomb porous structure then generated interfacial polarization loss. The doping of N atoms led to the increase in the number of dipole and defect sites regarded as polarization centers under electromagnetic fields, suitable for introducing large amounts of defective polarization and dipole polarization. Furthermore, the 3D honeycomb conductive structure of the shell layer contributed to conductive losses. The superior MA performance was issued from numerous loss mechanisms and high attenuation capability combined with excellent impedance matching benefited from the synergistic effect of the magnetic core and conductive shell, in particular, the improvement of impedance matching on the shell.

4. Conclusions

Porous honeycomb yolk-shell absorber with enhanced impedance matching, core diameter of 230–310 nm, shell thickness of 65 nm, honeycomb pore size of 2.3 nm, and doped nitrogen atoms in the carbon shell was successfully prepared. The MA properties indicated an attractive RL$_{min}$ value (-68.03 dB) of CoFe$_2$O$_4$@HCN microspheres at 2.5 mm. The absorber showed a broad EAB through the X and Ku bands of 4.52 GHz (change from 9.4 to 13.92 GHz). The RL$_{min}$ value maintained -58.34 dB with EAB broadening to 5.92 GHz (from 11.92 to 17.84 GHz) at 1.99 mm. The improved impedance matching and attenuation mechanisms of N-doped carbon revealed decreased effective dielectric constant, interfacial polarization, dipole polarization, and defective polarization, among others. In sum, yolk-shell structures with improved impedance matching are provided as a feasible strategy for the synthesis of future N-doped carbon materials.

Declaration of competing interest

The authors declare that they have no known competing financial interests or personal relationships that could have appeared to influence
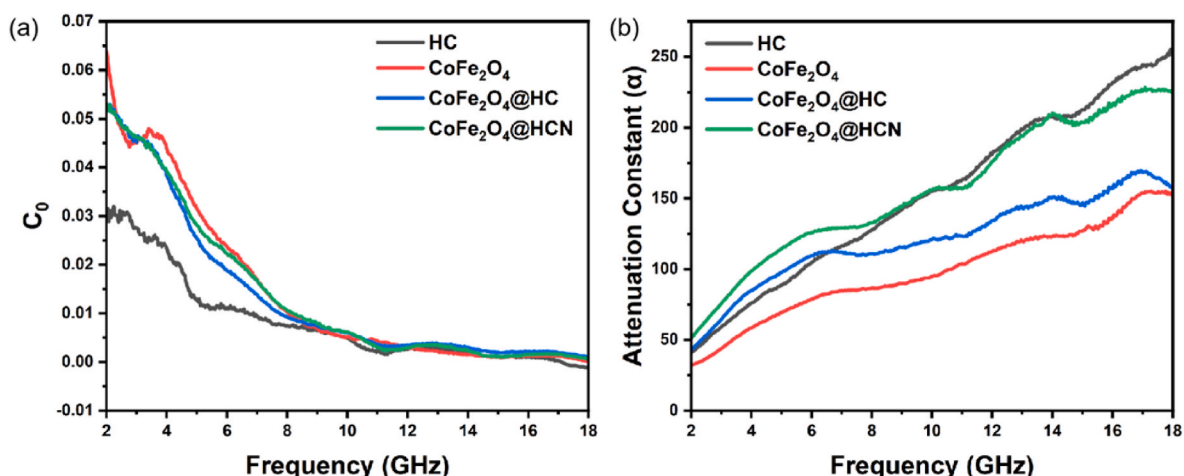

Fig. 9. (a) Eddy current loss coefficient and (b) attenuation constant (α) of HC, CoFe$_2$O$_4$, CoFe$_2$O$_4$@HC, and CoFe$_2$O$_4$@HCN.

the work reported in this paper.

Acknowledgment

The authors greatly acknowledge the financial support from the Scientific and Technological Development Program of Jilin Province (Grant No. 20220201138GX).

Appendix A. Supplementary data

Supplementary data to this article can be found online at https://doi.org/10.1016/j.ceramint.2023.03.297.

References

[1] D. Guan, G. Xu, Y. Sun, C.M. Sun, W.X. Zhou, W.J. Xu, H.W. Li, Urban electromagnetic environmental pollution and protection, Adv. Mater. Res. 726–731 (2013) 4190–4193. https://doi.org/10.4028/www.scientific.net/AMR.726-731.4190.

[2] G. Ding, C. Chen, H. Tai, Z. Tang, Z. Wang, G. Cheng, X. Wan, Structural characterization and microwave absorbing performance of CuFe$_2$O$_4$/RGO composites, J. Solid State Chem. 297 (2021), 122051, https://doi.org/10.1016/j.jssc.2021.122051.

[3] C. Chen, S. Bao, B. Zhang, Y. Chen, W. Chen, C. Wang, Coupling Fe@Fe$_3$O$_4$ nanoparticles with multiple-walled carbon nanotubes with width band electromagnetic absorption performance, Appl. Surf. Sci. 467–468 (2019) 836–843, https://doi.org/10.1016/j.apsusc.2018.10.148.

[4] H. Zhang, C. Shi, Z. Jia, X. Liu, B. Xu, D. Zhang, G. Wu, FeNi nanoparticles embedded reduced graphene/nitrogen-doped carbon composites towards the ultra-wideband electromagnetic wave absorption, J. Colloid Interface Sci. 584 (2021) 382–394, https://doi.org/10.1016/j.jcis.2020.09.122.

[5] Y. Duan, H. Pang, X. Wen, X. Zhang, T. Wang, Microwave absorption performance of FeCoNiAlCr$_{0.9}$ alloy powders by adjusting the amount of process control agent, J. Mater. Sci. Technol. 77 (2021) 209–216, https://doi.org/10.1016/j.jmst.2020.09.049.

[6] H. Pang, Y. Duan, L. Huang, L. Song, J. Liu, T. Zhang, X. Yang, J. Liu, X. Ma, J. Di, X. Liu, Research advances in composition, structure and mechanisms of microwave absorbing materials, Compos. B Eng. 224 (2021), 109173, https://doi.org/10.1016/j.compositesb.2021.109173.

[7] Y. Cui, Z. Liu, X. Li, J. Ren, Y. Wang, Q. Zhang, B. Zhang, MOF-derived yolk-shell Co@ZnO/Ni@NC nanocage: structure control and electromagnetic wave absorption performance, J. Colloid Interface Sci. 600 (2021) 99–110, https://doi.org/10.1016/j.jcis.2021.05.015.

[8] H. Cheng, Y. Pan, X. Wang, C. Liu, C. Shen, D.W. Schubert, Z. Guo, X. Liu, Ni flower/MXene-melamine foam derived 3D magnetic/conductive networks for ultra-efficient microwave absorption and infrared stealth, Nano-Micro Lett. 14 (1) (2022) 63, https://doi.org/10.1007/s40820-022-00812-w.

[9] H. Zhang, H. Wang, Y. Wang, B. Xin, Controlled synthesis and photocatalytic performance of biocompatible uniform carbon quantum dots with microwave absorption capacity, Appl. Surf. Sci. 512 (2020), 145751, https://doi.org/10.1016/j.apsusc.2020.145751.

[10] H. Sun, R. Che, X. You, Y. Jiang, Z. Yang, J. Deng, L. Qiu, H. Peng, Cross-stacking aligned carbon-nanotube films to tune microwave absorption frequencies and increase absorption intensities, Adv. Mater. 26 (48) (2014) 8120–8125, https://doi.org/10.1002/adma.201403735.

[11] Y. Duan, H. Pang, H. Zhang, Structure and composition design on ternary CNT@ZnFe$_2$O$_4$@ZnO composite utilized as enhanced microwave absorbing materials, Diam. Relat. Mater. 120 (2021), 108701, https://doi.org/10.1016/j.diamond.2021.108701.

[12] Y. Wang, D. Chen, X. Yin, P. Xu, F. Wu, M. He, Hybrid of MoS$_2$ and reduced graphene oxide: a lightweight and broadband electromagnetic wave absorber, ACS Appl. Mater. Interfaces 7 (47) (2015) 26226–26234, https://doi.org/10.1021/acsami.5b08410.

[13] X. Wang, J. Liao, R. Du, G. Wang, N. Tsidaeva, W. Wang, Achieving super-broad effective absorption bandwidth with low filler loading for graphene aerogels/raspberry-like CoFe$_2$O$_4$ clusters by N doping, J. Colloid Interface Sci. 590 (2021) 186–198, https://doi.org/10.1016/j.jcis.2021.01.069.

[14] W. Wang, Y. Wang, Z. Lu, R. Cheng, H. Zheng, Hollow ZnO/ZnFe$_2$O$_4$ microspheres anchored graphene aerogels as a high-efficiency microwave absorber with thermal insulation and hydrophobic performances, Carbon 203 (2023) 397–409, https://doi.org/10.1016/j.carbon.2022.11.103.

[15] J. Chen, X. Liang, W. Liu, W. Gu, B. Zhang, G. Ji, Mesoporous carbon hollow spheres as a light weight microwave absorbing material showing modulating dielectric loss, Dalton Trans. 48 (27) (2019) 10145–10150, https://doi.org/10.1039/c9dt01876j.

[16] P. Liu, T. Gao, W. He, P. Liu, Electrospinning of hierarchical carbon fibers with multi-dimensional magnetic configurations toward prominent microwave absorption, Carbon 202 (2023) 244–253, https://doi.org/10.1016/j.carbon.2022.10.089.

[17] N. Wang, Y. Wang, Z. Lu, R. Cheng, L. Yang, Y. Li, Hierarchical core-shell FeS$_2$/Fe$_7$S$_8$@C microspheres embedded into interconnected graphene framework for high-efficiency microwave attenuation, Carbon 202 (2023) 254–264, https://doi.org/10.1016/j.carbon.2022.10.083.

[18] H. Zhang, B. Wang, A. Feng, N. Zhang, Z. Jia, Z. Huang, X. Liu, G. Wu, Mesoporous carbon hollow microspheres with tunable pore size and shell thickness as efficient electromagnetic wave absorbers, Compos. B Eng. 167 (2019) 690–699, https://doi.org/10.1016/j.compositesb.2019.03.055.

[19] J. Chen, Y. Wang, Z. Gu, J. Huang, W. He, P. Liu, Rational design of hierarchical yolk-double shell Fe@NCNs/MnO$_2$ via thermal-induced phase separation toward wideband microwave absorption, Carbon 204 (2023) 305–314, https://doi.org/10.1016/j.carbon.2022.12.069.

[20] M. Ma, Y. Bi, Z. Jiao, J. Yue, Z. Liao, Y. Wang, Y. Ma, W. Huang, Facile fabrication of metal-organic framework derived Fe/Fe$_3$O$_4$/FeN/N-doped carbon composites coated with PPy for superior microwave absorption, J. Colloid Interface Sci. 608 (Pt 1) (2022) 525–535, https://doi.org/10.1016/j.jcis.2021.09.169.

[21] M. Ma, Z. Liao, X. Su, Q. Zheng, Y. Liu, Y. Wang, Y. Ma, F. Wan, Magnetic CoNi alloy particles embedded N-doped carbon fibers with polypyrrole for excellent electromagnetic wave absorption, J. Colloid Interface Sci. 608 (Pt 3) (2022) 2203–2212, https://doi.org/10.1016/j.jcis.2021.10.006.

[22] Y. Bi, M. Ma, Z. Jiao, Y. Ma, D. Hou, G. Geng, W. Feng, A. Ma, M. Qiao, Y. Liu, Enhancing electromagnetic wave absorption performance of one-dimensional C@Co/N-doped C@PPy composite fibers, Carbon 197 (2022) 152–162, https://doi.org/10.1016/j.carbon.2022.05.061.

[23] G. Cheng, F. Pan, X. Zhu, Y. Dong, L. Cai, W. Lu, Onion skin-derived hierarchical carbon/hollow CoFe$_2$O$_4$ composite with effective microwave absorption in multi-band, Compos. Commun. 27 (2021), 100867, https://doi.org/10.1016/j.coco.2021.100867.

[24] P. Liu, Y. Wang, G. Zhang, Y. Huang, R. Zhang, X. Liu, X. Zhang, R. Che, Hierarchical engineering of double-shelled nanotubes toward hetero-interfaces induced polarization and microscale magnetic interaction, Adv. Funct. Mater. 32 (33) (2022), https://doi.org/10.1002/adfm.202202588.

[25] C. Li, S. Ji, X. Jiang, G.I.N. Waterhouse, Z. Zhang, L. Yu, Microwave absorption by watermelon-like microspheres composed of γ-Fe$_2$O$_3$, microporous silica and polypyrrole, J. Mater. Sci. 53 (13) (2018) 9635–9649, https://doi.org/10.1007/s10853-018-2262-z.

[26] B. Wang, Y. Fu, J. Li, T. Liu, Yolk-shelled Co@SiO$_2$@Mesoporous carbon microspheres: construction of multiple heterogeneous interfaces for wide-bandwidth microwave absorption, J. Colloid Interface Sci. 607 (Pt 2) (2022) 1540–1550, https://doi.org/10.1016/j.jcis.2021.09.028.

[27] G. Wen, X. Zhao, Y. Liu, D. Yan, Z. Hou, Electromagnetic wave absorption performance and electrochemical properties of multifunctional materials: air@Co@Co$_3$Sn$_2$@SnO$_2$ hollow sphere/reduced graphene oxide composites, Chem. Eng. J. 420 (2021), 130479, https://doi.org/10.1016/j.cej.2021.130479.

[28] C. Tian, Y. Du, H. Xu, J. Xue, W. Chu, R. Qiang, X. Han, P. Xu, Differential shrinkage induced formation of yolk-shell carbon microspheres toward enhanced microwave absorption, Appl. Phys. Lett. 111 (13) (2017), https://doi.org/10.1063/1.4989750.

[29] Y. Jiang, X. Fu, R. Tian, W. Zhang, H. Du, C. Fu, Z. Zhang, P. Xie, J. Xin, R. Fan, Nitrogen-doped carbon nanofibers with sulfur heteroatoms for improving microwave absorption, J. Mater. Sci. 55 (14) (2020) 5832–5842, https://doi.org/10.1007/s10853-020-04430-y.

[30] J. Tao, J. Zhou, Z. Yao, Z. Jiao, B. Wei, R. Tan, Z. Li, Multi-shell hollow porous carbon nanoparticles with excellent microwave absorption properties, Carbon 172 (2021) 542–555, https://doi.org/10.1016/j.carbon.2020.10.062.

[31] B. Quan, X. Liang, G. Ji, Y. Zhang, G. Xu, Y. Du, Cross-linking-derived synthesis of porous Co$_x$Ni$_y$/C nanocomposites for excellent electromagnetic behaviors, ACS Appl. Mater. Interfaces 9 (44) (2017) 38814–38823, https://doi.org/10.1021/acsami.7b13411.

[32] Y. Wan, P. Zhu, S.-H. Yu, R. Sun, C.-P. Wong, W.-H. Liao, Graphene paper for exceptional EMI shielding performance using large-sized graphene oxide sheets and doping strategy, Carbon 122 (2017) 74–81, https://doi.org/10.1016/j.carbon.2017.06.042.

[33] L. Wang, H. Guan, Q. Huang, J. Hu, C. Dong, Y. Wang, Fe$_3$O$_4$/Fe/C composites prepared by a facile thermal decomposition method and their application as microwave absorbers, J. Alloys Compd. 784 (2019) 1123–1129, https://doi.org/10.1016/j.jallcom.2019.01.113.

[34] M. Zhang, J. Qiu, Z. Xin, X. Sun, In situ reduced multi-core yolk-shell Co@C nanospheres for broadband microwave absorption, Materials 14 (16) (2021) 4610, https://doi.org/10.3390/ma14164610.

[35] J. Pan, Y. Sun, Y. Wu, J. Li, W. Huang, K. Shi, Y. Lin, H. Dong, Q. Liu, Yolk-double shells hierarchical N-doped carbon nanosphere as an electrochemical nanoreactor for high performance lithium-sulfur batteries, Carbon 198 (2022) 80–90, https://doi.org/10.1016/j.carbon.2022.06.073.

[36] P. Liu, C. Zhu, S. Gao, C. Guan, Y. Huang, W. He, N-doped porous carbon nanoplates embedded with CoS$_2$ vertically anchored on carbon cloths for flexible and ultrahigh microwave absorption, Carbon 163 (2020) 348–359, https://doi.org/10.1016/j.carbon.2020.03.041.

[37] S. Wu, H. Liu, C. Yang, X. Li, Y. Lin, K. Yin, J. Sun, Q. Teng, C. Du, Y. Zhong, High-performance porous carbon catalysts doped by iron and nitrogen for degradation of bisphenol F via peroxymonosulfate activation, Chem. Eng. J. 392 (2020), 123683, https://doi.org/10.1016/j.cej.2019.123683.

[38] R. Yang, P. Reddy, C. Chang, P. Chen, J. Chen, C. Chang, Synthesis and characterization of Fe$_3$O$_4$/polypyrrole/carbon nanotube composites with tunable microwave absorption properties: role of carbon nanotube and polypyrrole content, Chem. Eng. J. 285 (2016) 497–507, https://doi.org/10.1016/j.cej.2015.10.031.

[39] R. Shu, C. Zhao, J. Zhang, W. Liu, X. Cao, Y. Li, S. Liu, Facile synthesis of nitrogen-doped reduced graphene oxide/nickel ferrite hybrid nanocomposites with superior electromagnetic wave absorption performance in the X-band, J. Colloid Interface Sci. 585 (2021) 538–548, https://doi.org/10.1016/j.jcis.2020.10.034.

[40] S. Wei, X. Wang, B. Zhang, M. Yu, Y. Zheng, Y. Wang, J. Liu, Preparation of hierarchical core-shell C@NiCo$_2$O$_4$@Fe$_3$O$_4$ composites for enhanced microwave absorption performance, Chem. Eng. J. 314 (2017) 477–487, https://doi.org/10.1016/j.cej.2016.12.005.

[41] Z. Wu, K. Tian, T. Huang, W. Hu, F. Xie, J. Wang, M. Su, L. Li, Hierarchically porous carbons derived from biomasses with excellent microwave absorption performance, ACS Appl. Mater. Interfaces 10 (13) (2018) 11108–11115, https://doi.org/10.1021/acsami.7b17264.

[42] X. Zhang, L. Cai, Z. Xiang, W. Lu, Hollow CuS microflowers anchored porous carbon composites as lightweight and broadband microwave absorber with flame-retardant and thermal stealth functions, Carbon 184 (2021) 514–525, https://doi.org/10.1016/j.carbon.2021.08.026.

[43] R. Mao, S. Bao, Q. Li, Y. Yuan, Z. Liang, M. Zhang, Z. Jiang, Z. Xie, Rational design of two-dimensional flaky Fe/void/C composites for enhanced microwave absorption properties, Dalton Trans. 51 (22) (2022) 8705–8713, https://doi.org/10.1039/d2dt01065h.

[44] M. Cao, W. Song, Z. Hou, B. Wen, J. Yuan, The effects of temperature and frequency on the dielectric properties, electromagnetic interference shielding and microwave-absorption of short carbon fiber/silica composites, Carbon 48 (3) (2010) 788–796, https://doi.org/10.1016/j.carbon.2009.10.028.

[45] J. Liu, J. Cheng, R. Che, J. Xu, M. Liu, Z. Liu, Double-Shelled yolk–shell microspheres with Fe$_3$O$_4$ cores and SnO$_2$ double shells as high-performance microwave absorbers, J. Phys. Chem. C 117 (1) (2012) 489–495, https://doi.org/10.1021/jp310898z.

[46] R. Che, L. Peng, X. Duan, Q. Chen, X. Liang, Microwave absorption enhancement and complex permittivity and permeability of Fe encapsulated within carbon nanotubes, Adv. Mater. 16 (5) (2004) 401–405, https://doi.org/10.1002/adma.200306460.

[47] W. Li, L. Wang, G. Li, Y. Xu, Single-crystal octahedral CoFe$_2$O$_4$ nanoparticles loaded on carbon balls as a lightweight microwave absorbent, J. Alloys Compd. 633 (2015) 11–17, https://doi.org/10.1016/j.jallcom.2015.02.006.

[48] K. Wang, Z. Ye, X. Li, J. Yang, Nanoporous resorcinol-formaldehyde based carbon aerogel for lightweight and tunable microwave absorption, Mater. Chem. Phys. 278 (2022), 125718, https://doi.org/10.1016/j.matchemphys.2022.125718.

[49] M. Qiao, X. Lei, Y. Ma, L. Tian, X. He, K. Su, Q. Zhang, Application of yolk–shell Fe$_3$O$_4$@N-doped carbon nanochains as highly effective microwave-absorption material, Nano Res. 11 (3) (2018) 1500–1519, https://doi.org/10.1007/s12274-017-1767-0.

[50] S. Wang, Y. Zhao, H. Xue, J. Xie, C. Feng, H. Li, D. Shi, S. Muhammad, Q. Jiao, Preparation of flower-like CoFe$_2$O$_4$@graphene composites and their microwave absorbing properties, Mater. Lett. 223 (2018) 186–189, https://doi.org/10.1016/j.matlet.2018.04.050.

[51] G. Shen, J. Ren, B. Zhao, B. Mei, H. Wu, X. Fang, Y. Xu, Magnetic hollow mesoporous carbon composites with impedance matching for highly effective microwave absorption, J. Mater. Sci. 54 (5) (2018) 4024–4037, https://doi.org/10.1007/s10853-018-3100-z.

[52] J. Wang, M. Zhou, Z. Xie, X. Hao, S. Tang, J. Wang, Z. Zou, G. Ji, Enhanced interfacial polarization of biomass-derived porous carbon with a low radar cross-section, J. Colloid Interface Sci. 612 (2022) 146–155, https://doi.org/10.1016/j.jcis.2021.12.162.

[53] Y. Du, W. Liu, R. Qiang, Y. Wang, X. Han, J. Ma, P. Xu, Shell thickness-dependent microwave absorption of core-shell Fe$_3$O$_4$@C composites, ACS Appl. Mater. Interfaces 6 (15) (2014) 12997–13006, https://doi.org/10.1021/am502910d.

[54] H. Lv, Z. Yang, P. Wang, G. Ji, J. Song, L. Zheng, H. Zeng, Z.J. Xu, A voltage-boosting strategy enabling a low-frequency, flexible electromagnetic wave absorption device, Adv. Mater. 30 (15) (2018), e1706343, https://doi.org/10.1002/adma.201706343.

[55] H. Jia, H. Xing, H. Ji, S. Gao, Self-template and in-situ polymerization strategy to lightweight hollow MnO$_2$@polyaniline core-shell heterojunction with excellent microwave absorption properties, Appl. Surf. Sci. 537 (2021), 147857, https://doi.org/10.1016/j.apsusc.2020.147857.

[56] C. Chen, S. Bao, B. Zhang, Y. Zhou, S. Li, Development of sulfide-doped Graphene/Fe$_3$O$_4$ absorber with wide band electromagnetic absorption performance, J. Alloys Compd. 770 (2019) 90–97, https://doi.org/10.1016/j.jallcom.2018.08.057.

[57] Z. Liao, M. Ma, Z. Tong, R. Wang, Y. Bi, Y. Chen, K.L. Chung, Y. Ma, Fabrication of ZnFe$_2$O$_4$/C@PPy composites with efficient electromagnetic wave absorption

[58] L. Wang, X. Yu, X. Li, J. Zhang, M. Wang, R. Che, Conductive-network enhanced microwave absorption performance from carbon coated defect-rich Fe$_2$O$_3$ anchored on multi-wall carbon nanotubes, Carbon 155 (2019) 298–308, https://doi.org/10.1016/j.carbon.2019.07.049.

[59] X. Liang, Z. Man, B. Quan, J. Zheng, W. Gu, Z. Zhang, G. Ji, Environment-stable Co$_x$Ni$_y$ encapsulation in stacked porous carbon nanosheets for enhanced microwave absorption, Nano-Micro Lett. 12 (1) (2020) 102, https://doi.org/10.1007/s40820-020-00432-2.

[60] X. Yang, Y. Duan, Y. Zeng, H. Pang, G. Ma, X. Dai, Experimental and theoretical evidence for temperature driving an electric-magnetic complementary effect in magnetic microwave absorbing materials, J. Mater. Chem. C 8 (5) (2020) 1583–1590, https://doi.org/10.1039/c9tc06551b.

[61] Y. Liu, T. Cui, T. Wu, Y. Li, G. Tong, Excellent microwave-absorbing properties of elliptical Fe$_3$O$_4$ nanorings made by a rapid microwave-assisted hydrothermal approach, Nanotechnology 27 (16) (2016), 165707, https://doi.org/10.1088/0957-4484/27/16/165707.

[62] H. Lv, G. Ji, X. Liang, H. Zhang, Y. Du, Porous three-dimensional flower-like Co/CoO and its excellent electromagnetic absorption properties, ACS Appl. Mater. Interfaces 7 (18) (2015) 9776–9783, https://doi.org/10.1021/acsami.5b01654.

[63] M. Zeng, J. Liu, M. Yue, H. Yang, H. Dong, W. Tang, H. Jiang, X. Liu, R. Yu, High-frequency electromagnetic properties of the manganese ferrite nanoparticles, J. Appl. Phys. 117 (2015), 17B527, https://doi.org/10.1063/1.4917515.

[64] H. Lv, G. Ji, X. Liang, H. Zhang, Y. Du, A novel rod-like MnO$_2$@Fe loading on graphene giving excellent electromagnetic absorption properties, J. Mater. Chem. C 3 (19) (2015) 5056–5064, https://doi.org/10.1039/c5tc00525f.

[65] Z. Yang, M. Li, Y. zhang, L. Yang, J. Liu, Y. Wang, Q. He, Constructing uniform Fe$_3$O$_4$@C@MnO$_2$ microspheres with yolk-shell interior toward enhancement in microwave absorption, J. Alloys Compd. 817 (2020), 152795, https://doi.org/10.1016/j.jallcom.2019.152795.

[66] H. Zhu, H. Liang, J. Chen, H. Chang, X. Jiao, Q. Jiao, C. Feng, H. Li, Y. Zhang, Y. Zhao, Rational construction of yolk-shell structured Co$_3$Fe$_7$/FeO@carbon composite and optimization of its microwave absorption, J. Colloid Interface Sci. 626 (2022) 775–786, https://doi.org/10.1016/j.jcis.2022.06.156.

[67] W. Dai, F. Chen, H. Luo, Y. Xiong, X. Wang, Y. Cheng, R. Gong, Synthesis of yolk-shell structured carbonyl iron@void@nitrogen doped carbon for enhanced microwave absorption performance, J. Alloys Compd. 812 (2020), 152083, https://doi.org/10.1016/j.jallcom.2019.152083.

[68] L. Chai, Y. Wang, N. Zhou, Y. Du, X. Zeng, S. Zhou, Q. He, G. Wu, In-situ growth of core-shell ZnFe$_2$O$_4$@porous hollow carbon microspheres as an efficient microwave absorber, J. Colloid Interface Sci. 581 (Pt B) (2021) 475–484, https://doi.org/10.1016/j.jcis.2020.07.102.

[69] J. Xu, R. Shu, Z. Wan, J. Shi, Construction of three-dimensional hierarchical porous nitrogen-doped reduced graphene oxide/hollow cobalt ferrite composite aerogels toward highly efficient electromagnetic wave absorption, J. Mater. Sci. Technol. 132 (2023) 193–200, https://doi.org/10.1016/j.jmst.2022.05.050.

[70] J. Wang, S. Hu, Q. Tang, J. Xu, N. Xu, S. Yu, X. Wang, H. Tian, One-pot hydrothermally prepared rGO/SiC/CoFe$_2$O$_4$ composites with strong microwave absorption at different thicknesses, Ceram. Int. 48 (20) (2022) 30640–30650, https://doi.org/10.1016/j.ceramint.2022.07.007.

[71] M.Z. Ashfaq, A. Ashfaq, M.K. Majeed, A. Saleem, S. Wang, M. Ahmad, M.M. Hussain, Y. Zhang, H. Gong, Confined tailoring of CoFe$_2$O$_4$/MWCNTs hybrid-architectures to tune electromagnetic parameters and microwave absorption with broadened bandwidth, Ceram. Int. 48 (7) (2022) 9569–9578, https://doi.org/10.1016/j.ceramint.2021.12.155.

[72] P. Yin, G. Wu, Y. Tang, S. Liu, Y. Zhang, G. Bu, J. Dai, Y. Zhao, Y. Liu, Structure regulation in N-doping biconical carbon frame decorated with CoFe$_2$O$_4$ and (Fe,Ni) for broadband microwave absorption, Chem. Eng. J. 446 (2022) 136975, https://doi.org/10.1016/j.cej.2022.136975.

[73] J. Luo, Y. Wang, Z. Qu, W. Wang, D. Yu, Anisotropic, multifunctional and lightweight CNTs@CoFe$_2$O$_4$/polyimide aerogels for high efficient electromagnetic wave absorption and thermal insulation, Chem. Eng. J. 442 (2022), 136388, https://doi.org/10.1016/j.cej.2022.136388.

[74] D. Zhang, W. He, G. Quan, Y. Wang, Y. Su, L. Lei, Y. Du, Y. Hong, S. Wang, Y. Tang, W. Zhang, Y. Chen, Sterculia lychnophora seed-derived porous carbon@CoFe$_2$O$_4$ composites with efficient microwave absorption performance, Appl. Surf. Sci. 607 (2023), 155027, https://doi.org/10.1016/j.apsusc.2022.155027.